

# Influence of interstitial Mn on magnetism in room-temperature ferromagnet $\text{Mn}_{1+\delta}\text{Sb}$

A. E. Taylor,<sup>1,\*</sup> T. Berlijn,<sup>2</sup> S. E. Hahn,<sup>3</sup> A. F. May,<sup>4</sup> T. J. Williams,<sup>1</sup> L. Poudel,<sup>1,5</sup> S. Calder,<sup>1</sup>  
R. S. Fishman,<sup>4</sup> M. B. Stone,<sup>1</sup> A. A. Aczel,<sup>1</sup> H. B. Cao,<sup>1</sup> M. D. Lumsden,<sup>1</sup> and A. D. Christianson<sup>1,5</sup>

<sup>1</sup>Quantum Condensed Matter Division, Oak Ridge National Laboratory, Oak Ridge, Tennessee 37831, USA

<sup>2</sup>Center for Nanophase Materials Sciences and Computer Science and Mathematics Division,  
Oak Ridge National Laboratory, Oak Ridge, TN 37831-6494, USA

<sup>3</sup>Neutron Data Analysis and Visualization Division,  
Oak Ridge National Laboratory, Oak Ridge, Tennessee 37831, USA

<sup>4</sup>Materials Science and Technology Division, Oak Ridge National Laboratory, Oak Ridge, Tennessee 37831, USA

<sup>5</sup>Department of Physics and Astronomy, University of Tennessee, Knoxville, TN 37996, USA

We report elastic and inelastic neutron scattering measurements of the high- $T_C$  ferromagnet  $\text{Mn}_{1+\delta}\text{Sb}$ . Measurements were performed on a large,  $T_C = 434\text{K}$ , single crystal with interstitial Mn content of  $\delta \approx 0.13$ . The neutron diffraction results reveal that the interstitial Mn has a magnetic moment, and that it is aligned antiparallel to the main Mn moment. We perform density functional theory calculations including the interstitial Mn, and find the interstitial to be magnetic in agreement with the diffraction data. The inelastic neutron scattering measurements reveal two features in the magnetic dynamics: i) a spin-wave-like dispersion emanating from ferromagnetic Bragg positions (HK  $2n$ ), and ii) a broad, non-dispersive signal centered at forbidden Bragg positions (HK  $2n+1$ ). The inelastic spectrum cannot be modeled by simple linear spin-wave theory calculations, and appears to be significantly altered by the presence of the interstitial Mn ions. The results show that the influence of the interstitial Mn on the magnetic state in this system is more important than previously understood.

PACS numbers: 75.50.Cc, 75.25.-j, 71.15.Mb, 78.70.Nx

## INTRODUCTION

$\text{Mn}_{1+\delta}\text{Sb}$  is a high Curie temperature ( $T_C$ ), highly anisotropic, metallic ferromagnet. The observation of a ferromagnetic state in  $\text{Mn}_{1+\delta}\text{Sb}$  is unusual in its class of materials. Most Mn-alloys are antiferromagnetic, and other 3d transition metal mono-antimonides are not ferromagnetic — CrSb, FeSb and CoSb are antiferromagnetic, TiSb is paramagnetic and NiSb is diamagnetic [1]. The ferromagnetic state in  $\text{Mn}_{1+\delta}\text{Sb}$  is highly sensitive to substitutions; for example, Cr-doping quickly tunes the system towards an antiferromagnetic state [2, 3]. In-fact substitutions of the cation, the anion, or presence of an interstitial can each alter  $T_C$ , the magnetic anisotropy, or the type of magnetic order [2–9]. This potential for tuning the properties in  $\text{Mn}_{1+\delta}\text{Sb}$ , and closely related  $\text{Mn}_{1+\delta}\text{Bi}$ , has attracted considerable attention because the materials show promise as alternatives to rare-earth containing permanent magnets, and as magneto-optic mediums [10–18].

The spontaneous magnetization in  $\text{Mn}_{1+\delta}\text{Sb}$  is along the crystallographic  $c$ -axis at high temperatures. However, the anisotropy decreases on cooling and passes through zero at the spin reorientation temperature,  $T_{SR}$ , so that the magnetization is in-plane at low temperatures. In nominally  $\delta = 0$  polycrystalline MnSb the  $T_C$  is as high as  $T_C = 587\text{K}$  [19]. However, single crystal studies have been unable to produce the material without the inclusion of interstitial Mn ions [8]. These in-

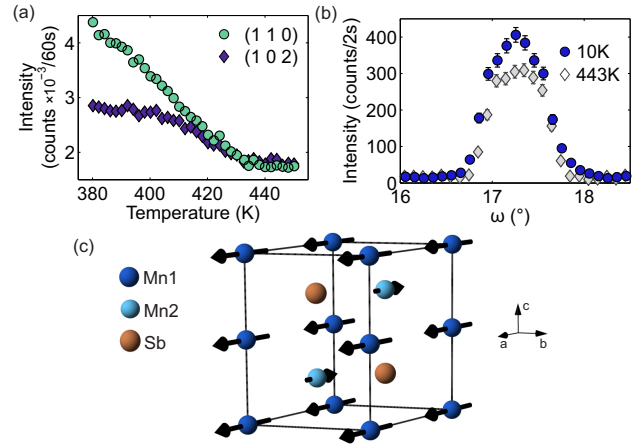


Figure 1. (Color online) (a) Temperature dependence of the peak intensity at the (110) (circles) and (102) (diamonds) Bragg positions across  $T_C$  measured on HB-3A. Error bars are smaller than the size of the markers. (b) The (103) Bragg peak measured at 10 K [circles] and 443 K [diamonds] as a function of goniometer angle  $\omega$ , which rotates the crystal in the scattering plane. (c) One unit cell showing the low temperature ( $T < T_{SR}$ ) magnetic structure of  $\text{Mn}_{1+\delta}\text{Sb}$ . The interstitial sites are shown here as fully occupied.

terstitial Mn ions, Mn2, are present in addition to the fully-occupied main site Mn ions, Mn1. The Mn2 ions are hosted within the hexagonal NiAs crystal structure as shown in Fig. 1(c). Compositions in the range of  $\delta \approx 0.05 - 0.2$  have been found to be stable.

The presence of interstitials significantly alters the properties of  $\text{Mn}_{1+\delta}\text{Sb}$ . As  $\delta$  increases, the  $a$  lattice

\* taylorae@ornl.gov

parameter and unit cell volume increase, but the  $c$  lattice parameter,  $T_C$ ,  $T_{SR}$  and the total magnetization decrease [5, 8, 9]. Studies combining magnetization measurements with chemical analysis [8, 20] found that the interstitial Mn results in a reduction of the ferromagnetic ordering temperature as captured in a simple relationship between  $T_C$  and  $\delta$ :

$$T_C = (577 - 900 \times \delta) \text{ K}. \quad (1)$$

The electronic structure and magnetic state of  $\text{Mn}_{1+\delta}\text{Sb}$  have been investigated by a number of authors via electronic structure calculations [12, 13, 21–24]. They found that MnSb is described as a metallic system with localized magnetic moments, and show that the ferromagnetic state is stabilized due to the significant hybridization between the Mn  $3d$  and Sb  $5p$  orbitals. All these calculations, however, have failed to describe key experimental observations such as the behavior of the magnetic anisotropy [23], and the effect of the interstitial Mn on the magnetic properties [12]. Coehoorn *et al.* [12] simply discuss Mn2 as an electron donor, and were unable to explain its influence on the magnetic properties.

Given the importance of the interstitials in tuning the properties of  $\text{Mn}_{1+\delta}\text{Sb}$ , it is surprising that detailed theoretical investigations of the effect of Mn2 are lacking. Experimental results are also limited, and have focused on the empirical determination of the  $\delta$  dependencies of cell parameters,  $T_C$  and  $T_{SR}$ . This is probably due to a prevailing view in the literature that there is no magnetic moment associated with Mn2. This perspective originated from the analysis of polarized neutron diffraction data [25, 26], using a model with a complex aspherical magnetic form factor for Mn1. A large asymmetry in the form factor allows the Mn1 site to contribute magnetic intensity to Bragg reflections that would otherwise be forbidden for Mn1 scattering. In these analyses, low- $Q$  Bragg peaks had to be excluded to model the data. Analysis of powder neutron diffraction data [27, 28], x-ray Compton profile measurements [29], and electronic structure calculations [12] raised questions as to how robust the aspherical magnetic form factor model is. Additionally, a density functional theory (DFT) calculation on the influence of Pt doping in MnBi did include Mn at the interstitial site, created via a vacancy on a main Mn site, and predicted a magnetic moment of order  $-3 \mu_B$  associated with the interstitial site [16]. The absence of Mn2 from most calculations may be attributable to the inherent difficulty in including a partially occupied, disordered arrangement of interstitial ions into calculations. The role of the interstitial Mn in determining the magnetic properties of  $\text{Mn}_{1+\delta}\text{Sb}$ , therefore, is an open question which could provide key insights into the material properties and tunability.

Here we show that the presence of the interstitial Mn ion has a strong influence on the magnetic state of  $\text{Mn}_{1+\delta}\text{Sb}$ , beyond the role of a simple electron donor. We use neutron diffraction to measure a large number of Bragg peaks from a  $\delta = 0.13$  single crystal sample at

temperatures above and below both  $T_C$  and  $T_{SR}$ . We find that the data is described across the entire  $Q$ -range by a simple model including a magnetic moment on the Mn2 site, aligned antiparallel to the moment on the Mn1 site. We perform DFT calculations including an interstitial Mn, and find these to carry a sizable magnetic moment in agreement with our diffraction results. The DFT results are also consistent with the observed reduction in  $T_C$  due to the presence of Mn2. We also investigate the magnetic dynamics of  $\text{Mn}_{1+\delta}\text{Sb}$  via inelastic neutron scattering (INS) measurements performed on a large single crystal. We identify a spin-wave-like signal associated with the ferromagnetic Mn1 ions, and are able to partially reproduce its dispersion using a localized-moment Heisenberg model. In addition to the spin-wave-like scattering, we also identify a broad, intense, magnetic response in the inelastic spectrum. This signal is not observed in  $\delta = 0$  MnBi, and therefore is likely attributable to the presence of the interstitials in  $\text{Mn}_{1.13}\text{Sb}$ . These results highlight the strong influence that the presence of the interstitial Mn has on the magnetic properties of  $\text{Mn}_{1+\delta}\text{Sb}$ .

## EXPERIMENTAL TECHNIQUES

The single crystal of  $\text{Mn}_{1+\delta}\text{Sb}$  used in this investigation is the same  $\sim 6 \text{ cm}^3$  crystal that was studied in Ref. [30]. Pieces taken from the large crystal were used for diffraction and magnetization measurements.

To determine the spin reorientation temperature, a piece of the crystal was aligned at room temperature to within  $15^\circ$  of the easy axis ( $c$ -axis) using a permanent magnet. The magnetization ( $\mathbf{M}$ ) was then measured in a Quantum Design Magnetic Property Measurement System, with applied fields  $\mathbf{H}$  either parallel or perpendicular to this axis. This measurement clearly reveals a spin reorientation temperature of  $\sim 160 \text{ K}$ , as shown in Fig. 2(a). The same crystal was then used to obtain the Curie temperature of  $434 \text{ K}$ , see Fig. 2(b). This high-temperature measurement employed the Sample Space Oven from Quantum Design, which utilizes thin quartz holders that precluded alignment of the crystal. Here, we have defined  $T_C$  as the intercept of the greatest tangent to the  $M/H$  versus  $T$  data, with the greatest tangent being observed at  $423 \text{ K}$ . According to Eq. 1,  $T_C = 434 \text{ K}$  gives an interstitial content of 16 %, consistent with the value predicted from the lattice parameters in Ref. [30]. With an applied field of  $6 \text{ T}$ , the moment is essentially saturated at  $2 \text{ K}$ , and for  $\mathbf{H} \perp c$  we measure a saturated moment of  $3.20 \mu_B/\text{f.u.}$ , where f.u. is a formula unit  $\text{Mn}_{1.13}\text{Sb}$ . The high-temperature data shows a minor onset of magnetization at  $T \sim 580 \text{ K}$ , see Fig. 2(b). This is likely associated with a small close-to-stoichiometric MnSb impurity, or a small amount of an unknown phase.

Neutron diffraction measurements were performed on the HB-3A four-circle diffractometer at the High Flux Isotope Reactor (HFIR) at Oak Ridge National Labo-

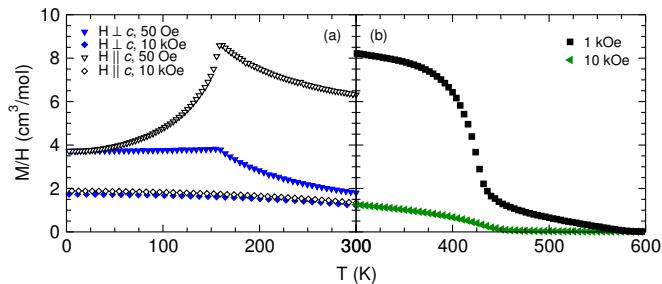


Figure 2. (Color online) Magnetization data showing the two magnetic transitions, with (a) revealing the spin reorientation at 160 K by examining data collected on an oriented crystal, and (b) demonstrating the bulk Curie temperature near 434 K. All of the data were collected while cooling in an applied field, except for the 10 kOe data that were collected on the first warming measurement above 300 K.

ratory (ORNL), using a neutron wavelength of 1.003 Å. Full datasets of more than 190 reflections were collected at temperatures of 10 K ( $<T_{SR}$ ), 200 K ( $T_{SR} < 200 \text{ K} < T_C$ ) and 450 K ( $>T_C$ ), in a closed-cycle refrigerator (CCR). 450 K data were counted for 2 s per point and 200 K and 10 K data were counted 5 s per point. In addition, a set of 10 peaks, which are predicted by model 1 (see Results section) to be highly sensitive to the direction of the interstitial moment with respect to the Mn1 site moment, were counted for up to 60 s per point at all temperatures.

INS measurements were performed on the SEQUOIA spectrometer at the Spallation Neutron Source (SNS), ORNL with the crystal aligned with (H 0 L) in the scattering plane. Measurements were performed with an incident energy ( $E_i$ ) of 150 meV with chopper frequency of  $f = 300 \text{ Hz}$ , and with  $E_i = 60 \text{ meV}$  and  $f = 180 \text{ Hz}$ . This gave energy resolutions at the elastic line of 11 meV and 4 meV, respectively. A CCR was used to reach sample temperatures between 10 K and 443 K. Full data sets were collected at 10 K, 350 K and 443 K with  $E_i = 150 \text{ meV}$  over at least a  $130^\circ$  range of sample rotation angles with a step size of  $0.5^\circ$ . Limited angular range data sets with  $1^\circ$  step size were collected at 40 K, 100 K, 125 K, 150 K, 170 K, 200 K, 250 K and 300 K. Measurements were performed with  $E_i = 60 \text{ meV}$  at 10 K and 350 K over an  $80^\circ$  range with a  $2^\circ$  step size. The angular step data were combined, a slight misorientation of the crystal was corrected for, and cuts through the data were performed using the Horace software package [31]. Additional INS measurements were performed on the US/Japan Cold Neutron Triple-Axis Spectrometer (CTAX) at HFIR, ORNL, using guide-open-80'-open collimation and fixed final neutron energy of 5 meV.

## RESULTS

### Neutron diffraction

Results from the neutron diffraction measurements are shown in Fig. 1. The temperature dependencies of (110) and (102) Bragg reflections across  $T_C$  are shown in Fig. 1(a). These reflections have structure factor contributions from all three atoms in the unit cell. The intensities of these Bragg peaks respond to  $T_C$ , indicating that they are magnetic Bragg reflections, and confirming the identification of  $T_C$  from magnetization. Figure 1(b) shows the (103) Bragg reflection at 443 K and 10 K. The Mn1 site in the NiAs crystal structure has the reflection condition  $l = 2n$ , where  $n$  is an integer. Therefore, the (103) peak has zero nuclear contribution to its structure factor from Mn1, and also zero magnetic contribution if the magnetic form factor of Mn1 is spherical. Both Mn2 and Sb ions contribute scattering intensity to the (103) reflection.

To determine the origin of the increased intensity at low temperature of  $l = \text{odd}$ ,  $(h-k) \neq 3n$  Bragg peaks, we investigated two possible models for the magnetic state in  $\text{Mn}_{1+\delta}\text{Sb}$  for all reflections collected. Both models use the NiAs structure, hexagonal space group  $P6_3/mmc$  (No. 194), which has two formula units of  $\text{Mn}_{1+\delta}\text{Sb}$  per unit cell, with Mn1 on the  $2a$  Wyckoff site (000), Sb on the  $2c$  Wyckoff site ( $\frac{1}{3} \frac{2}{3} \frac{1}{4}$ ), and Mn2 on the  $2d$  Wyckoff site ( $\frac{1}{3} \frac{2}{3} \frac{3}{4}$ ). We use standard Miller indices (h k l) to index the reflections. Note that because of the hexagonal symmetry the Miller-Bravais notation can be used to illustrate equivalent reflections, given by (h k i l) where  $i = -(h+k)$  and permutations of h k i give equivalent reflections [32]. Recent x-ray diffraction results from the closely related compound MnBi identify a slight distortion from hexagonal symmetry below  $T_{SR}$ , however the resolution of our neutron diffraction measurement is not sufficient to detect a distortion of this size [33]. The difference between the two models we investigate concerns the magnetic component of scattering below  $T_C$ .

The first model comprises a ferromagnetic arrangement of Mn1 moments, with Mn2 moments aligned antiparallel to Mn1. A depiction of this model is shown in Fig. 1(c) for  $T < T_{SR}$ , i.e. with spins aligned within the  $a$ - $b$  plane. For  $T > T_{SR}$  the Mn1 and Mn2 moments are aligned along the  $c$ -axis, but still antiparallel to each other. The  $3d$ - $5p$  hybridization is expected to induce a small moment on the Sb site antiparallel to Mn1 [12]. However, considering the expected moment size and the steep magnetic form factor for Sb  $5p$  electrons [25], the overall contribution of Sb to the magnetic diffraction pattern is expected to be small. Therefore we do not include magnetic intensity from Sb in the fitting for either model 1 or model 2, consistent with previous reports [25–27]. As Sb and Mn2 have the same reflection conditions, this may have the effect of slightly increasing the moment size assigned to the interstitial Mn.

The model was fit to the data using Rietveld refine-

ment in the FullProf software suite [34]. For a random distribution of interstitial Mn ions, the average structure can be modeled by assuming a uniform distribution of Mn2 on every  $2d$  Wyckoff site and scaling the scattering intensity by the occupancy  $\delta$ . The atomic displacement parameters for Sb and Mn2 were constrained to be equal, as they contribute to the same reflections. The initial fit was performed against the  $T = 450$  K (i.e.  $T > T_C$ ) data set, allowing us to determine the interstitial content of the sample without the influence of magnetic Bragg scattering. The standard empirical correction for extinction used in FullProf was utilised in this refinement [34], resulting in an extinction coefficient of 580(60) which gives a maximum extinction correction of 68% on the strongest Bragg peak. Using this fitting procedure the value of the interstitial content was determined to be  $\delta = 0.13(1)$ , which is reasonably close to the value estimated from comparison of the magnetization measurement (see Fig. 2) to Eq. 1. For subsequent fits of the magnetic model against 10 K and 200 K data sets the interstitial content and the extinction parameter were kept fixed. The magnetic form factor of  $\text{Mn}^{2+}$  was used [26, 35]. For the 10 K data set, the model included three domains in equal proportions with spins along  $a$ ,  $b$ , and  $[-1 -1 0]$  directions respectively. The results of these fits are summarized in Fig. 3(a), (b) and (c) and Table I. Excellent agreement between data and model 1 is found.

To highlight the magnetic component of the scattering, Fig. 3(e) shows a comparison of the 10 K data minus the calculated structural component of the scattering, with the calculated magnetic contribution to the scattering. The intensity of the magnetic contribution is seen to decrease with  $Q$  for both data and calculation, as expected due to the magnetic form factor. The effects of the structure factor and polarization factor, which selects scattering from only moments perpendicular to  $Q$ , in the neutron scattering cross section are present in this data, which is why there is not an exact form factor dependence. In addition, some forbidden Bragg positions were measured and appear at zero integrated intensity. Attempts to fit an interstitial Mn moment aligned parallel to Mn1, instead of antiparallel, were unsuccessful. The model with an antiparallel moment on the Mn2 site describes the data very well.

The second model is based on that proposed by Haneda *et al.* [36] for MnAs and discussed in detail for MnSb by Yamaguchi *et al.* [25], in which Mn2 does not have a magnetic moment associated with it. In this case, they explain the observed magnetic scattering at  $(103)$  and other  $l = \text{odd}$  Bragg positions [25–27] using a highly aspherical magnetic form factor for the main site Mn. Having an aspherical magnetization density breaks the symmetry conditions that normally result in systematic absences for  $l = \text{odd}$  reflections from the  $2a$  Wyckoff site, allowing intensity at  $l = \text{odd}$ ,  $(h - k) \neq 3n$  positions. The model includes the combined scattering intensity for structural contributions from all ions, plus the magnetic intensity from the Mn1 ions for all reflections. We have

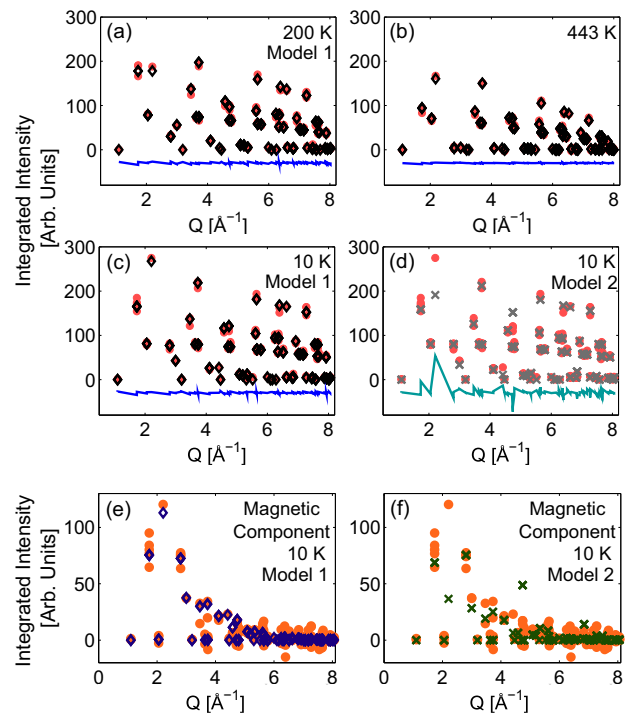


Figure 3. (Color online) Results of model 1 fitted in FullProf compared to (a) 200 K, (b) 443 K and (c) 10 K data. (d) Model 2 compared to 10 K data. The data points (red circles) are the integrated intensities of peaks in scans similar to those shown in Fig. 1(b) for all measured Bragg positions. The results predicted from model 1 (open diamonds), and model 2 (crosses) are shown. The difference between the data and models (solid lines) have been offset from zero for clarity. (e) and (f) Show the extracted magnetic component of the scattering. The data minus the calculated structural part of the scattering are plotted (orange circles), along with the calculated magnetic component of the scattering for model 1 (open diamonds) and model 2 (crosses).

added to model 2 the same extinction correction as used in model 1. The overall structure factor resulting from the Yamaguchi model, with adjusted interstitial content and electron occupancies to match our data, is compared to the 10 K data in Fig. 3(d). For this model we find  $\chi^2 = 2.49$  and  $R_F = 6.21$ , compared with  $\chi^2 = 2.46$  and  $R_F = 4.55$  for model 1 at 10 K (Table I). The purely magnetic component of model 2 is shown in Fig. 3(f), along with the difference between the data and calculated structural component. In this case there is significant deviation between the model and the data over a large range of  $Q$ , with the intensities of only some magnetic peaks being replicated. Therefore model 2 is not as effective as model 1 in describing the results of our neutron diffraction experiment. This will be examined further in the Discussion Section.

Temperature (K)	$a$ (Å)	$c$ (Å)	Vol. (Å <sup>3</sup> )	$M_{\text{Mn1}}$ (μ <sub>B</sub> )	$M_{\text{Mn2}}$ (μ <sub>B</sub> )	ext	scale	$\chi^2$	$R_{\text{F}}$
450 K	4.193(3)	5.773(4)	87.9(1)	–	–	580(60)	346(7)	0.325	3.79
200 K	4.195(6)	5.723(8)	87.2(2)	2.92(4) [   $c$ ]	-1.4(3) [   $c$ ]	580	368(5)	2.45	4.05
10 K	4.189(5)	5.690(7)	86.5(2)	3.54(2) [ $\perp$ $c$ ]	-2.5(1) [ $\perp$ $c$ ]	580	372(6)	2.46	4.55

Table I. Results from Rietveld refinements fitting model 1 to the data. Vol. is volume of the unit cell,  $M_{\text{Mn1}}$  and  $M_{\text{Mn2}}$  are the magnitudes of the magnetic moments on Mn1 and Mn2 sites respectively, ext and scale are the extinction and scale factors and  $\chi^2$  and  $R_{\text{F}}$  are the statistical agreement factors determined by FullProf.  $\chi^2$  is low for the 450 K data set because of the shorter collection time used for this data set. The errors on the moment sizes are the estimated standard deviation calculated by FullProf.

### DFT calculations

To gain a better understanding of the influence of the Mn interstitials on  $\text{Mn}_{1+\delta}\text{Sb}$  we performed DFT calculations including an interstitial in the unit cell (see [37] for technical details). First we readdress the question of whether the interstitial Mn has a magnetic moment, and if so how it is directed with respect to the ferromagnetically aligned moments of the host Mn atoms. To this end we considered the  $2 \times 2 \times 1$  supercell  $\text{Mn}_9\text{Sb}_8$  depicted in Fig. 4, which contains a single interstitial Mn atom. To account for the influence of Coulomb interactions among the Mn-3d electrons we use the PBE+U approximation, and vary the Hubbard  $U$  parameter between 0 and 8 eV. For all cases, we find that it is not possible to stabilize a configuration in which the interstitial Mn is non-magnetic. The tables in Fig. 4 show that for  $U = 0, 2$  and 4 eV the configuration with Mn2 aligned parallel to Mn1 is higher in energy than the configuration in which it is aligned antiparallel, consistent with the results from neutron diffraction. For  $U = 6$  and 8 eV, however, the configuration with the parallel alignment of the interstitial Mn is energetically favored. It is reasonable to expect that the Coulomb  $d$ - $d$  interactions are at the lower end of the scale, given that the very large wave functions of the Sb  $5p$  electrons can effectively screen the transition metal interactions. Related to this, we find for all cases that the system remains metallic, even for a Hubbard  $U$  of 8 eV.

Next we examine the effect of the Mn interstitials on the ferromagnetic configuration of the host Mn moments. To investigate the stability of the ferromagnetic ground state (FM) we compare its energy with that of two higher energy configurations in which the atomic positions remain unchanged, but the host Mn moments assume an antiferromagnetic configuration either along the  $c$ -axis (AFM- $c$ ) or the  $a$ -axis (AFM- $a$ ) as shown in Fig. 5. Comparing Fig. 5(a) and (c), the presence of the Mn interstitial lowers the energy difference between the FM ground state and the high energy AFM configurations. The energy difference between the FM and the AFM- $c$  configuration reduces quite significantly from 286 to 212 meV and the energy difference between the FM and the AFM- $a$  configuration decreases from 326 to 306 meV. The results in Fig. 5 are for a  $U = 2$  eV, but for a  $U$  of 8 eV we find that this qualitative conclusion remains

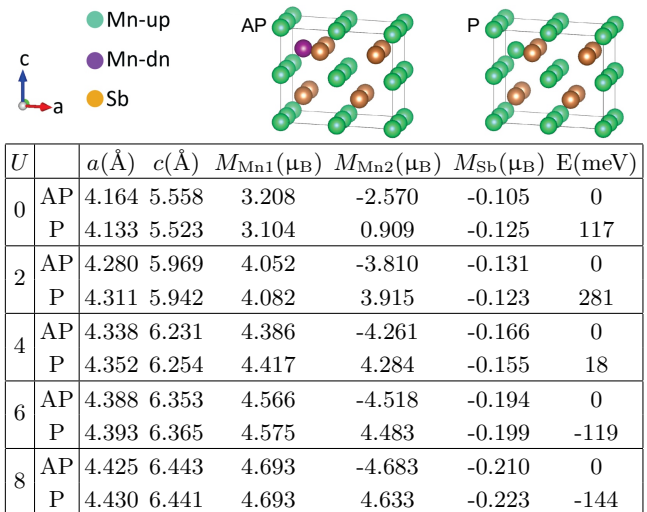


Figure 4. (Color online) The optimized lattice constants, the average host Mn1 moment, the interstitial Mn2 moment, the average Sb moment, and the total energy per interstitial Mn2 atom of the parallel (P) and antiparallel (AP) configuration of Mn2 calculated within the PBE+U approximation for  $U=0,2,4,6$  and 8 eV.

unchanged [38].

It is important to note that the simulations in Fig. 5(a) and (c) include the indirect influence of Mn2 via their induced changes in the lattice constants. From comparing the lattice parameters between the undoped and doped system in Fig. 5(a) and (c) we see that, just like in the experimental observations [9], the Mn interstitials tend to increase the  $a$  lattice parameter while decreasing the  $c$  lattice parameter. This leads to the question of whether the change in lattice parameters is solely responsible for the damaging influence of the Mn interstitials on the FM state. To address that question, we present in Fig. 5(b) the stability of the FM state again, for a system which has the strained lattice parameters of the doped system but does not include the Mn interstitials. The energy differences of this undoped strained system shown in Fig. 5(b) differ significantly from those in the doped system shown in Fig. 5(c). This illustrates that Mn2 affects the ferromagnetic state not just via the change of lattice parameters, suggesting that the magnetic exchange interactions between the host and the interstitial Mn moments and/or



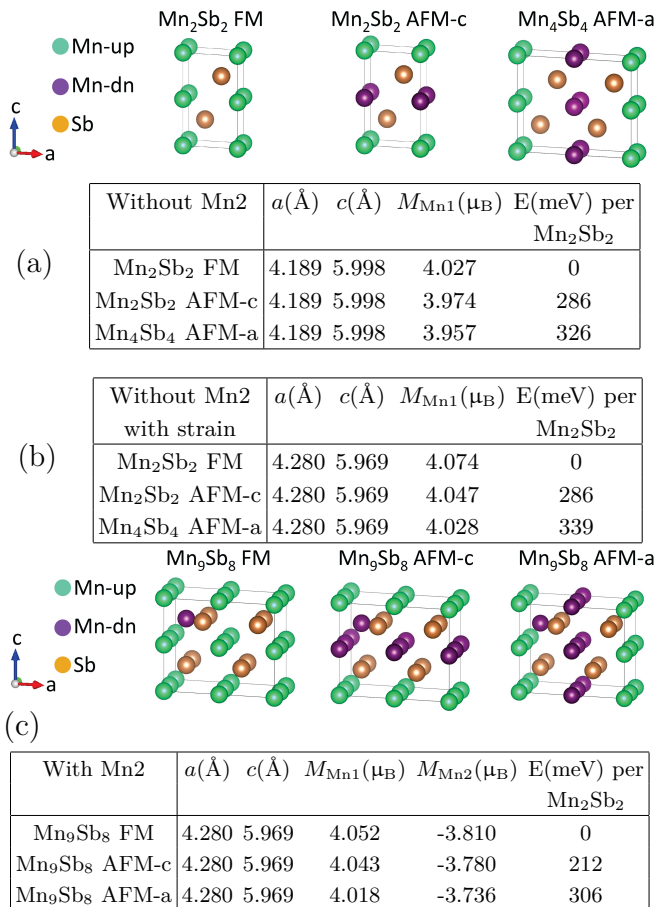


Figure 5. (Color online) The lattice constants, the average of the absolute value of the host Mn1 moments, the interstitial Mn2 moment and the total energy per  $\text{Mn}_2\text{Sb}_2$  unit cell of the FM, AFM-c and AFM-a configurations for the cases without ((a) and (b)) and with ((c)) an interstitial Mn2 atom, calculated within the PBE+U approximation with  $U=2$  eV. The lattice constants and internal parameters for the cases (a) and (c) are obtained from optimizing the  $\text{Mn}_2\text{Sb}_2$ -FM/ $\text{Mn}_9\text{Sb}_8$ -FM configuration, respectively. In (b) the lattice constants from the configuration with Mn2 are used in the unit cells without Mn2, giving effective strained lattice constants.

doping effects play an important role. Previous attempts to explain the magnetic properties of  $\text{Mn}_{1+\delta}\text{Sb}$  just via doping effects were not successful [12].

### Inelastic neutron scattering

To investigate the magnetic state in  $\text{Mn}_{1.13}\text{Sb}$  further, we performed INS experiments to probe the magnetic dynamics. An overview of the results from SEQUOIA is given in Figs. 6(a) and 7, which show HL-plane and  $QE$ -plane color maps, respectively, as well as constant-energy cuts through the data in Fig. 7(d). These inelastic scattering spectra contain contributions from both magnetic and phonon scattering. However, the phonon scattering contribution is effectively negligible in the results

we present. Mn and Sb have nuclear scattering cross sections of opposite sign, therefore their scattering contributions largely cancel-out and as a result the acoustic phonon scattering from the sample is weak. Additionally, the phonon intensity follows a  $Q^2$  dependence and is therefore weak in the low- $Q$  zones we investigate. In the low temperature data the phonon scattering is suppressed by the Bose-population factor in the energy range investigated, whereas at higher temperature phonons (attributable to both sample and background contributions) simply result in an overall increase in the background scattering, particularly at low energies, as evident in Fig. 6(a). Therefore the results presented are attributable to the magnetic dynamics of  $\text{Mn}_{1+\delta}\text{Sb}$ .

In Fig. 6(a) rings of scattering in the HL plane are seen dispersing with energy out of the ferromagnetic positions such as (100) and (002); compare to Fig. 6(c) which depicts the (H0L) reciprocal lattice plane. Only  $L = \text{even}$  positions are magnetic zone centers because the Mn1 magnetic lattice is half the size of the structural lattice along the  $c$ -axis, see Fig. 1(c). The rings persist above both  $T_{\text{SR}}$  and  $T_{\text{C}}$ . The intensity of the rings is rapidly suppressed with increasing  $Q$  at all temperatures, and it persists up to energies of  $\sim 70$  meV (see Fig. 7(a)), well above the phonon cutoff of the sample  $\sim 30$  meV, indicating the magnetic origin of the signal. We observe this signal down to low energies in the data from our measurement on CTAX, Fig. 8. This shows that the dispersion of the magnetic signal along H can already be observed out of (100) with an energy transfer of 0.5 meV, see Fig. 8. This dispersive signal is reasonably reproduced by a spin-wave Heisenberg model for Mn1 ions, presented in Fig 9, discussed further below, and a qualitatively similar signal is observed in MnBi [39], which contains no interstitial Mn, see Fig. 6(b).

In the inelastic spectra, in addition to the spin-wave type signal, a broad signal is evident between the rings in the HL plane at all temperatures, see Fig. 6(a). This broad signal was not observed in MnBi, corroborating that it is a distinct feature of the excitation spectrum of  $\text{Mn}_{1+\delta}\text{Sb}$ , Fig. 6(b). The broad signal is centered on (001) and equivalent positions. (001) is not an allowed Bragg reflection in this system (see Fig. 6(c)), and no Bragg peak was observed at this position in any of the measurements we performed. Figure 7(c) highlights that this signal is broad but localized in  $Q$ -space, and seemingly non-dispersive. Again, the intensity suppression with  $Q$  and the energy range of the signal at all temperatures both indicate that it is magnetic in origin. We observe this signal down to the lowest energies we were able to resolve in our experimental set-up on SEQUOIA,  $\sim 4$  meV, but are unable to determine if there is an associated elastic diffuse signal. This signal was previously observed at (101) in the triple-axis-spectroscopy work of Radhakrishna and Cable [30], but we have now been able to map its full  $Q$  and  $E$  dependence and confirm the signal's magnetic origin, in addition to observing it at (001).

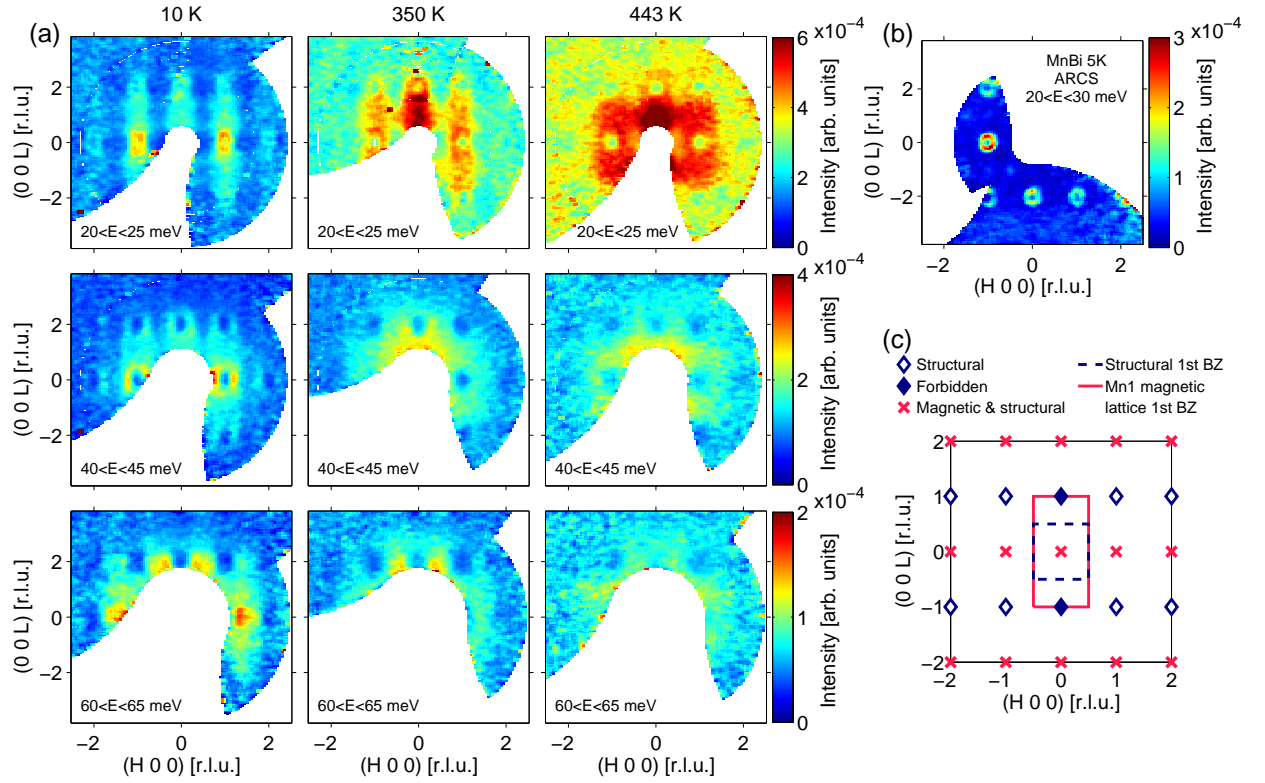


Figure 6. (Color online) (a) Neutron scattering intensity maps of  $\text{Mn}_{1+\delta}\text{Sb}$  in the HL-plane. The data were acquired on SEQUOIA at 10 K, 200 K and 443 K, as indicated, with  $E_i = 150$  meV. Slices were averaged over the energy ranges indicated and over  $\pm 0.1$  reciprocal lattice units [r.l.u.] in the  $(0.5\xi -\xi\ 0)$  direction (perpendicular to  $(H\ 0\ 0)$  and  $(0\ 0\ L)$ ). The data on interstitial-free MnBi in (b) was taken on the ARCS spectrometer at the SNS, at a temperature of 5 K and with  $E_i = 80$  meV, courtesy of Ref. [39]. (c) A map of reciprocal space for  $\text{Mn}_{1+\delta}\text{Sb}$  indexed on the structural unit cell. The first Brillouin Zones (BZs) of the structural unit cell (dashed line), and the magnetic unit cell of the Mn1 ions (solid line) are shown. Structural (diamonds and crosses) and Mn1 magnetic lattice (crosses) Bragg positions are indicated, with systematically absent reflections shown as closed diamonds.

Further investigation of the scattering centered on  $(0\ 0\ 1)$  is presented in Fig. 10. Cuts taken along  $(1\ 0\ L)$  and  $(H\ 0\ 1)$  directions through datasets collected at 10 K, 350 K and 443 K are shown in Fig. 10(a) and (b). As the  $(H\ 0\ 1)$  direction is the zone boundary for the spin wave signal (see Fig. 6(c)) the cuts in Fig. 10(b) and the color map in Fig. 7(c) essentially show the broad signal in isolation. The  $(1\ 0\ L)$  direction, however, passes through the zone center for both the spin wave and the broad signal, therefore both are observed in Figs. 10(a) and 7(d). We show the temperature dependence of the  $(0\ 0\ 1)$  signal in Fig. 10(c). The integrated intensity was determined from cuts made along the  $(H\ 0\ 1)$  direction through the limited-angular-range data measured at  $E_i = 150$  meV for all temperatures. The data were averaged over 10–20 meV and folded along H and L to improve statistics. Two Gaussian functions on a flat background were fit to the data, with widths constrained to be equal, but amplitudes varying independently, and centers fixed at  $H=0$  and  $H=1$ . The resulting area of the Gaussian centered at  $H=0$  was corrected for the Bose population factor,  $[1 - \exp(-E/k_B T)]^{-1}$ , at each temperature and the re-

sult gives the integrated intensity plotted in Fig. 10(c).

These results show that the broad,  $\mathbf{Q} = (0\ 0\ 1)$ -centered scattering is influenced by  $T_{\text{SR}}$ , Fig. 10(c). There is a dramatic increase in intensity of the signal on warming past  $T_{\text{SR}}$ , which is expected for scattering from a transverse magnetic fluctuation as the spins reorient from  $ab$ -plane to  $c$ -axis alignment, because the magnetic cross section depends only on the component of the magnetic moment perpendicular to  $\mathbf{Q}$ . This is further supported by the observation that the  $(0\ 0\ 1)$  scattering is more sensitive to  $T_{\text{SR}}$  than the scattering at  $(\pm 1\ 0\ 1)$ , compare the cuts in Fig. 10(b). These observations are a further confirmation of the magnetic origin of the signal, and indicate coupling between this scattering and the ferromagnetic state of the system.

### Spin-wave modelling

We attempted to model the inelastic magnetic response of the system using linear spin-wave theory. Isotropic exchange interactions including up to sixth nearest neigh-

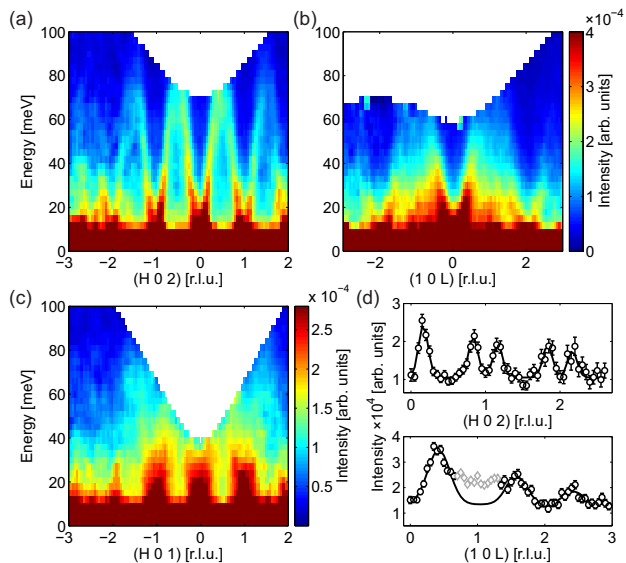


Figure 7. (Color online) (a-c) Neutron scattering intensity maps for  $\text{Mn}_{1+\delta}\text{Sb}$  from data taken on SEQUOIA with  $E_i = 150 \text{ meV}$  at 10 K. The data were averaged over  $\pm 0.1 \text{ r.l.u.}$  in the two  $\mathbf{Q}$ -space directions perpendicular to the  $x$ -axis in each case. (d) Markers show constant-energy cuts through the data shown in (a) and (b), averaged over 20–25 meV. Solid lines show the result of fitting Gaussians plus a flat background to the data. The gray diamonds in the (1 0 L) cut show the region of data excluded from the fit, as this region is dominated by the broad (0 0 1) type scattering from the (1 0 1) position.

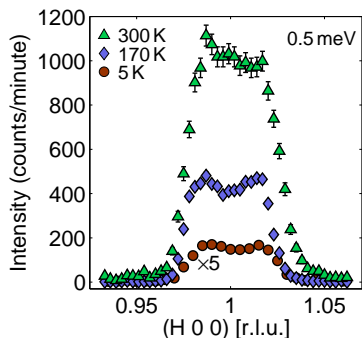


Figure 8. (Color online) Low energy data measured on CTAX along the (H 0 0) direction through ferromagnetic position (1 0 0). Measurements were made with energy transfer of 0.5 meV at 5, 170 and 300 K, as indicated. The data have been normalized to number of counts per minute. The 5 K data has been multiplied by 5 for clarity.

bors were the minimum required to model the spin-wave frequencies. The six nearest neighbor exchange parameters,  $J_s$ , are illustrated in Fig. 9(c). Single-ion anisotropy was not included because there was no evidence for a gap in the spin-wave spectrum down to at least 0.5 meV ( $< 1\%$  of the bandwidth), see Fig. 8. The inelastic neutron cross section for undamped spin waves was calculated using the  $1/S$  formalism outlined in Ref. 40 and

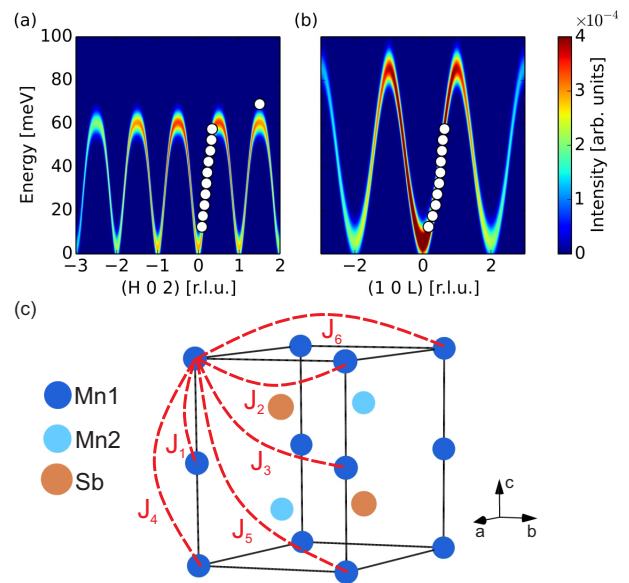


Figure 9. (Color online) Spin-wave dispersion calculated for the H-direction (a) and L-direction (b), with calculated intensities corresponding to (H 0 2) and (1 0 L) directions, respectively. The white circles are the points extracted from cuts through the data (see Fig. 7(d) and text) that were used to fit the model parameters. (c) Depiction of exchange constants used in the Heisenberg model, from 1st to 6th nearest neighbors for Mn1 ions.

appendix A of Ref. 41. For comparison with experimental intensities, the effects of the magnetic form factor and an approximation for the instrumental resolution were included in the calculation. We used the magnetic form factor for  $\text{Mn}^{2+}$  from Ref. 35. The resolution function was approximated as a Gaussian in energy with a full width at half-maximum of 7.5 meV and the results averaged over the same volume of  $\mathbf{Q}$  as the experimental data (Fig. 7) and averaged over six domains. To determine the exchange parameters, the model was fit to the dispersions along (1 0 0), (0 0 1) and (1 1 0) directions, extracted from the experimental data via a series of constant-energy cuts and fits like those in Fig. 7(d). We determined the energy at the (H 0 2) zone boundary, 70(4) meV, by fitting a Gaussian to a constant- $\mathbf{Q}$  cut at (1.5 0 2) from which a similar cut at (2 0 2) had been subtracted as a background.

The results of this modeling are shown in Fig. 9(a) and (b), which show reasonable correspondence to the spin-wave data presented in Fig. 7(a) and (b). However, the bandwidth of the dispersion does not appear to be well reproduced along the H direction, see Fig. 9(a). Only  $J_6$  can be uniquely determined from our results. Instead,



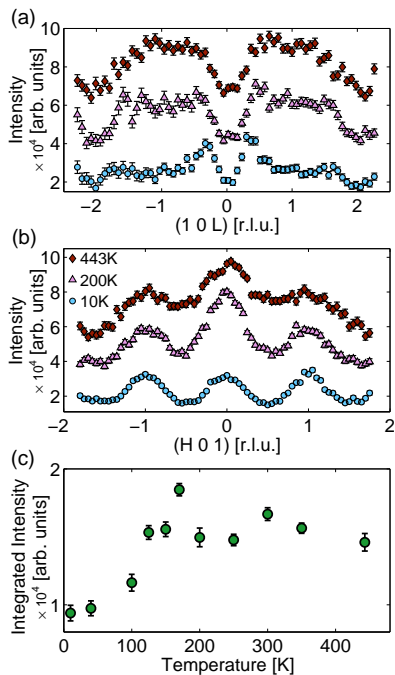


Figure 10. (Color online) (a) and (b) Constant-energy cuts averaged over 20–25 meV from  $E_i = 150$  meV SEQUOIA data measured at 10 K (circles), 200 K (triangles) and 443 K (diamonds). Cuts in (a) were averaged over  $\pm 0.1$  r.l.u. in perpendicular  $\mathbf{Q}$ -space directions, and successive cuts were offset  $2 \times 10^{-4}$  for clarity. Cuts in (b) were averaged over  $\pm 0.2$  r.l.u. in perpendicular  $\mathbf{Q}$ -space directions. (c) shows the temperature dependence of the signal centered on (001), determined from (H 0 1) cuts as described in the text. The plotted integrated intensity has been corrected for the Bose population factor.

the linear combinations

$$\begin{aligned}\alpha &= J_1 + 6J_3 \\ \beta &= J_4 + 6J_5 \\ \gamma &= J_2 + 2J_3 + 2J_5\end{aligned}$$

were fit. The values best fitting these measurements are  $\alpha S = 20.0$  meV,  $\beta S = -0.8$  meV,  $\gamma S = 4.8$  meV, and  $J_6 S = 2.9$  meV. Fig. 9 shows the calculated frequencies and intensities along two of the measured directions, for comparison to Fig. 7(a) and (b). Previously Refs. [42] and [30] reported triple-axis spectroscopy measurements on  $\text{Mn}_{1+\delta}\text{Sb}$  which covered limited ranges of  $\mathbf{Q}$  and  $E$ , not reaching the zone boundary. In Ref [42] they fit a Heisenberg model up to fourth nearest neighbors (i.e.  $J_5 = J_6 = 0$  for comparison to our model) to the low energy data measured on a  $\text{Mn}_{1.05}\text{Sb}$  crystal. They found  $\alpha S = 8.75$  meV,  $\beta S = 2.4$  meV and  $\gamma S = 5.4$  meV. These results extrapolate to a bandwidth of 130 meV along (H 0 2), which is much larger than the 70(4) meV we observe, see Fig. 7.

## DISCUSSION

### Magnetic Structure

The results of our neutron diffraction experiment on  $\text{Mn}_{1.13}\text{Sb}$  are well described by the magnetic structure shown in Fig. 1(c), with ferromagnetic alignment of Mn1 ions, and Mn2 ions aligned antiparallel to Mn1. There appears to be no need to include the model of an aspherical form factor for Mn1 to account for magnetic scattering at  $l = \text{odd}$ ,  $(h - k) \neq 3n$  Bragg peak positions for our data set. This is consistent with early neutron powder diffraction results on  $\text{Mn}_{1+\delta}\text{Sb}$  [27], but in contrast to the interpretations of Yamaguchi *et al.* [25] and Reimers *et al.* [26] from their polarized-neutron, single-crystal experiments.

The single crystals investigated in Refs. [25] and [26] were of composition  $\text{Mn}_{1.05}\text{Sb}$  and  $\text{Mn}_{1.09}\text{Sb}$  respectively, lower interstitial contents than our crystal, and in both cases they excluded some low  $Q$  data from their analysis. This may explain the seeming discrepancy between their interpretation and our results. In the former case, the scattering from Mn2 sites would have been weaker, and therefore harder to interpret. The higher  $Q$  data that they included in their analysis is less sensitive to magnetic scattering from the interstitial site, but more sensitive to the asymmetric form factor they describe. In the case of our data, only model 1, including an antiparallel moment on Mn2, can account for all peaks observed below  $T_C$  across all  $Q$ , see Fig. 3(c)–(f). Our data is less sensitive to any asymmetry in the Mn1 form factor because it was not a polarized neutron measurement and the magnetic contribution at high  $Q$  is small. Our results do not preclude some asphericity in the magnetic form factor of Mn1. It is likely, however, that the asphericity found in the previous models is too large, as some of the scattering intensity should have been accounted for by the moment on Mn2. This helps to explain the discrepancies between the Yamaguchi model [25] and results from x-ray Compton profile analysis [29], and electronic structure calculations [12], as well as the failure of the model at low  $Q$  [20, 25, 26].

The size of the magnetic moments found from our Full-Prof refinement of model 1 are consistent with magnetization measurements. The saturated moment per formula unit was found to be  $3.20 \mu_B$  at 2 K from magnetization. The results from HB-3A give a total moment per formula unit of  $3.2(1) \mu_B$  at 10 K, taking into account the Mn2 occupancy of  $\delta = 0.13(1)$ , see Table I. The determination of a magnetic moment associated with the Mn2 site is further supported by the results from our DFT calculation. Previous modeling of  $\text{Mn}_{1+\delta}\text{Sb}$  did not include an interstitial Mn, and those that attempted to account for it merely adjusted the electron count in stoichiometric MnSb models [5, 13, 21–24, 43, 44]. We find a sizable moment on Mn2 in the calculation, see Fig. 4.

Given the presence of a magnetic moment on the interstitial site, in a simple local Heisenberg picture we

would expect the antiparallel alignment of the interstitial to enhance the overall ferromagnetic state. However, it has clearly been observed that the presence of the interstitial acts to reduce  $T_C$  [5, 8, 9]. Our DFT calculation shows that the interstitial Mn degrades the stability of the ferromagnetic state beyond the simple influence of changing lattice parameters (see Fig. 5), in agreement with the experimental observations. This indicates that a purely localized moment model may not be sufficient to describe the magnetic state in  $\delta \neq 0$   $\text{Mn}_{1+\delta}\text{Sb}$ .

### Magnetic Dynamics

Our inelastic neutron scattering measurements of  $\text{Mn}_{1+\delta}\text{Sb}$  serve to highlight the influence the interstitial Mn has on the magnetic state. The spin-wave-type excitations appear to be less well defined than in the non-interstitial containing sister compound MnBi (see Fig. 6), and are modified such that a simple Heisenberg model does not describe the observed dispersion. For a local moment system, linear spin-wave theory is expected to capture the form of the dispersion by inclusion of a small number of nearest neighbor exchange parameters. Although the observed dispersion (e.g. Fig. 7 (a)) appears to be associated with the ferromagnetic wavevector, and a similar feature is observed in interstitial-free MnBi (Fig. 6(b) [39]), we have shown that the measurement is not fully described by the Heisenberg model for localized Mn1 spins, Fig. 9.

For the spin wave calculation along (H 0 2), attempting to match both the bandwidth and the gradient of the dispersion at lower energies requires a large  $J_6$  interaction (2.9 meV), which probably reflects the inadequacy of the model. The shape at the zone boundary remains quite different, resulting in the 70(4) meV bandwidth not being reproduced, see Fig. 9(a). The calculation does not produce a signal emanating from (0 0 1) as is observed in the data, see Fig. 7(c). As (H 0 1) is a zone boundary for the Mn1 magnetic lattice, as illustrated in Fig. 6(c), the spin-wave intensity at (0 0 1) is concentrated around the zone boundary energy  $E = 85 \text{ meV}$  (see Fig. 9(b)). Our crude attempts to extend the model to include an interstitial Mn2 moment failed to better reproduce the spin wave data, nor did they produce a signal like the observed scattering along (0 0 1). These attempts are limited at the present time by the absence of general theoretical and computational tools to include the effects of a disordered component in a system on the inelastic magnetic response. Including a small moment at one interstitial site in our model calculation artificially introduces a symmetry element which is not present in the real system. Extending the calculation to include thousands of unit cells, which can then be randomly assigned interstitials, is currently difficult to implement and extremely computationally intensive.

In addition to the spin wave, we identified a second magnetic signal in the inelastic spectrum which is broad

in  $Q$ , and centered on an unexpected position in reciprocal space  $\mathbf{Q} = (0 0 1)$  (see Figs. 6, 7 and 10). Like the spin-wave scattering, this signal responds to  $T_{\text{SR}}$ , but unlike the spin-wave scattering, no similar signal is observed in interstitial-free MnBi. (0 0 1) is not an allowed nuclear or magnetic reflection (for either magnetic structure model discussed above). The presence of a (0 0 1) Bragg peak would require the correspondence between the upper and lower halves of the unit cell shown in Fig. 1(c) to be broken, for example, if Mn1 was antiferromagnetically aligned along  $c$ , or if Mn2 was only present in the lower half of the cell. We do not observe a Bragg peak at (0 0 1) in any of the neutron data sets collected, implying that no such long-range order is present. However, the periodicity of the signal in reciprocal space implies that underlying long-range correlations are present.

Our results show that the dynamic correlations observed at (0 0 1) are not associated with a long-range order in the system. They could, however, be associated with a short-range structural or magnetic order in the system. This proposition may be supported by the broad appearance of the signal in reciprocal space (see Fig. 6), which suggests a short correlation length in real space. We made a rough estimate for the correlation length by fitting Gaussians to cuts similar to those in Fig. 10(a) and (b), integrated over 10–15 meV, from the  $E_i = 60 \text{ meV}$ ,  $T = 10 \text{ K}$  data. We find correlation lengths of  $\sim 16 \text{ \AA}$  in the  $a$ - $b$  plane, and in the range 10–18  $\text{\AA}$  along  $c$  (where it is harder to define, due to the overlap of the signal with the spin-wave-type scattering), i.e.  $\sim 4$  unit cells in plane, and  $\sim 3$  units cells along  $c$ . We were unable to determine whether there is an elastic, diffuse scattering signal at the (0 0 1) position due to the neutron instrumentation used in this investigation. We do observe the signal down to the lowest energies that were probed on SEQUOIA,  $\sim 4 \text{ meV}$ . A short-range order could be present in the system if the interstitial Mn ions are not randomly distributed, but instead are structurally ordered over a few unit cells. An observation of elastic, diffuse scattering at (0 0 1) would establish that short-range order is present. Alternatively, the presence of interstitials could modify the interactions of neighboring main-site Mn1 ions, with the associated magnetic excitations unable to propagate over large length scales due to disruption from a random distribution of magnetic Mn2 ions. Further studies, including diffuse neutron scattering experiments, are highly desirable to investigate the potential short-range order in this system.

The spectral weight of the (0 0 1) scattering, i.e. the total intensity of the signal integrated over  $\mathbf{QE}$  space, can in principle be used to indicate the strength of the magnetic excitations and therefore the size of the fluctuating magnetic moment, which could give an indication of the origin of the scattering. Unfortunately, due to the overlap of the two magnetic excitations in  $\mathbf{QE}$  space, we cannot quantitatively compare the spectral weights of the two signals. Qualitatively, however, by inspecting a series of slices and cuts through the data, such as those shown in

Figs. 6, 7 and 10, we see that the strength of the signal emanating from (001) is comparable to the spin-wave signal. This implies that the (001) signal is associated with a relatively large magnetic moment per formula unit in the sample, of the order of the Mn1 moment size. This makes it unlikely to be purely the result of the Mn2 moments behaving independently of Mn1. Identification of the origin of this signal would be extremely significant for understanding the magnetic state in  $\text{Mn}_{1+\delta}\text{Sb}$  and determining the possibilities of tuning the state with interstitial ions of Mn or other 3d transition metals.

## CONCLUSIONS

We have shown that a magnetic moment on the interstitial Mn in  $\text{Mn}_{1+\delta}\text{Sb}$  is required to describe the neutron diffraction data from a single crystal of  $\text{Mn}_{1.13}\text{Sb}$ . This magnetic moment is aligned antiparallel to the main site Mn magnetic moment. We performed DFT calculations which find that the interstitial Mn is magnetic, consistent with the diffraction data. The DFT results are also consistent with previous experimental evidence that the interstitial reduces  $T_C$  and  $c$  lattice parameter, and increases  $a$  in  $\text{Mn}_{1+\delta}\text{Sb}$ . We find that the presence of the magnetic interstitial Mn also has a substantial effect on the magnetic excitation spectrum of  $\text{Mn}_{1+\delta}\text{Sb}$ , measured by inelastic neutron scattering. It results in the appearance of an intense, broad signal in  $Q$ -space, that is likely associated with short-range order. While a Heisenberg Hamiltonian model calculation captures the essential  $Q$ -space dependence of the spin-wave type signal observed, the additional broad signal cannot be explained by straightforward attempts to include an interstitial ion

in this model.

## ACKNOWLEDGEMENTS

We thank J. Q. Yan, D. Mandrus, M. A. McGuire and B. C. Sales for useful discussions. The research at ORNL's Spallation Neutron Source and High Flux Isotope Reactor was supported by the Scientific User Facilities Division, Office of Basic Energy Sciences, U.S. Department of Energy (DOE). A.F.M. and R.F. were supported by the U.S. DOE, Office of Science, Basic Energy Sciences, Materials Sciences and Engineering Division. T.B. and T.J.W. are supported as Wigner Fellows at ORNL. Work by TB was performed at the Center for Nanophase Materials Sciences, a DOE Office of Science user facility. This research used resources of the National Energy Research Scientific Computing Center, a DOE Office of Science User Facility supported by the Office of Science of the U.S. DOE under Contract No. DE-AC02-05CH11231. S.E.H. acknowledges support by the Laboratory's Director's fund, ORNL.

This manuscript has been authored by UT-Battelle, LLC under Contract No. DE-AC05-00OR22725 with the U.S. Department of Energy. The United States Government retains and the publisher, by accepting the article for publication, acknowledges that the United States Government retains a non-exclusive, paid-up, irrevocable, world-wide license to publish or reproduce the published form of this manuscript, or allow others to do so, for United States Government purposes. The Department of Energy will provide public access to these results of federally sponsored research in accordance with the DOE Public Access Plan (<http://energy.gov/downloads/doe-public-access-plan>).

- 
- [1] K. Motizuki, H. Ido, T. Itoh, and M. Morifuji, *Electronic Structure and Magnetism of 3d-Transition Metal Pnictides* (Springer Science & Business Media, 2009).
  - [2] W. J. Takei, D. E. Cox, and G. Shirane, *Phys. Rev.* **129**, 2008 (1963).
  - [3] H. Kohnke, C. Kleeberg, V. Dankelmann, K. Bärner, and J. Schünemann, *J. Alloy Compd* **239**, 150 (1996).
  - [4] H. J. Kohnke, V. Dankelmann, C. Kleeberg, J. W. Schünemann, K. Bärner, A. Vetcher, and G. A. Govor, *Phys. Stat. Sol. (b)* **191**, 511 (1995).
  - [5] T. Chen, D. Rogowski, and R. M. White, *J. Appl. Phys.* **49**, 1425 (1978).
  - [6] W. Reimers, E. Hellner, W. Treutmann, and G. Heger, *J. Phys. C: Solid State Phys.* **15**, 3597 (1982).
  - [7] J. Nakamura, Y. Kobayashi, F. Ambe, K. Asai, and N. Yamada, *Hyperfine Interact.* **68**, 311 (1992).
  - [8] T. Okita and Y. Makino, *J. Phys. Soc. Jpn.* **25**, 120 (1968).
  - [9] I. Teramoto and A. Van Run, *J. Phys. Chem. Solids* **29**, 347 (1968).
  - [10] K. Anand, J. Pulikkotil, and S. Auluck, *J. Magn. Magn. Mater.* **363**, 18 (2014).
  - [11] R. Carey, B. Thomas, and G. Bains, *J. Magn. Magn. Mater.* **83**, 21 (1990).
  - [12] R. Coehoorn, C. Haas, and R. A. de Groot, *Phys. Rev. B* **31**, 1980 (1985).
  - [13] A. Continenza, S. Picozzi, W. T. Geng, and A. J. Freeman, *Phys. Rev. B* **64**, 085204 (2001).
  - [14] G. Di, S. Iwata, S. Tsunashima, and S. Uchiyama, *J. Magn. Magn. Mater.* **104-107**, 1023 (1992).
  - [15] Y.-K. Hong, J. Park, O. N. Mryasov, S.-G. Kim, S. Kim, J. Lee, G. S. Abo, C.-J. Choi, and J. Lee, *AIP Advances* **3**, 052137 (2013).
  - [16] P. Kharel, R. Skomski, P. Lukashev, R. Sabirianov, and D. J. Sellmyer, *Phys. Rev. B* **84**, 014431 (2011).
  - [17] N. A. Zarkevich, L.-L. Wang, and D. D. Johnson, *APL Materials* **2**, 032103 (2014).
  - [18] Y. Ashizawa, S. Saito, and M. Takahashi, *J. Appl. Phys.* **91**, 8240 (2002).
  - [19] C. Guillaud, *Ann. Phys-Paris* **4**, 671 (1949).
  - [20] Y. Yamaguchi, H. Watanabe, and T. Suzuki, *J. Phys. Soc. Jpn.* **41**, 703 (1976).

- [21] K. Katoh, A. Yanase, and K. Motizuki, *J. Magn. Magn. Mater.* **54-57**, 959 (1986).
- [22] R. Podlucky, *Solid State Commun.* **50**, 763 (1984).
- [23] P. Ravindran, A. Delin, P. James, B. Johansson, J. M. Wills, R. Ahuja, and O. Eriksson, *Phys. Rev. B* **59**, 15680 (1999).
- [24] N. Vast, B. Siberchicot, and P. G. Zerah, *J. Phys.: Condens. Matter* **4**, 10469 (1992).
- [25] Y. Yamaguchi, H. Watanabe, and T. Suzuki, *J. Phys. Soc. Jpn.* **45**, 846 (1978).
- [26] W. Reimers, E. Hellner, W. Treutmann, and P. Brown, *J. Phys. Chem. Solids* **44**, 195 (1983).
- [27] J. Bouwma, C. F. van Bruggen, C. Haas, and B. van Laar, *Le Journal de Physique Colloques* **32**, C1 (1971).
- [28] Y. Yamaguchi and H. Watanabe, *J. Magn. Magn. Mater.* **31-34**, 619 (1983).
- [29] J. Nakamura, T. Takeda, K. Asai, N. Yamada, Y. Tanaka, N. Sakai, M. Ito, A. Koizumi, and H. Kawata, *J. Phys. Soc. Jpn.* **64**, 1385 (1995).
- [30] P. Radhakrishna and J. W. Cable, *Phys. Rev. B* **54**, 11940 (1996).
- [31] Horace: Software for visualising and manipulating  $S(\mathbf{Q}, \omega)$  measured in all four dimensions. T. G. Perring *et al.* <http://horace.isis.rl.ac.uk>.
- [32] F. C. Frank, *Acta Crystallographica* **18**, 862 (1965).
- [33] M. A. McGuire, H. Cao, B. C. Chakoumakos, and B. C. Sales, *Phys. Rev. B* **90**, 174425 (2014).
- [34] J. Rodríguez-Carvajal, *Physica B* **192**, 55 (1993).
- [35] A.-J. Dianoux and G. Lander, *Neutron Data Booklet*, 2nd ed. (Institut Laue-Langevin, 2003).
- [36] S. Haneda, N. Kazama, Y. Yamaguchi, and H. Watanabe, *J. Phys. Soc. Jpn.* **42**, 1201 (1977).
- [37] We employ the plane wave projector augmented wave (PAW) method [45] as implemented in the VASP code [46–48]. Atomic relaxations are converged down to 1 meV/Å. The number of plane waves is determined by an energy cut-off of 650 eV. For the  $\text{Mn}_2\text{Sb}_2$ ,  $\text{Mn}_4\text{Sb}_4$  and  $\text{Mn}_9\text{Sb}_8$  unit cells a  $8 \times 8 \times 5$ ,  $4 \times 8 \times 5$  and  $4 \times 4 \times 5$  k-mesh is employed respectively. For the PBE+U calculations the double counting correction scheme by Dudarev *et al.* [49] is used. Atomic images were produced with the VESTA program [50].
- [38] For  $U = 8$  eV we find that the energy difference between the FM and the AFM-c configuration reduces from 212 to 156 meV and the energy difference between the between the FM and the AFM-a configuration lowers from 219 to 185 meV.
- [39] T. J. Williams *et. al*, unpublished.
- [40] J. T. Haraldsen and R. S. Fishman, *J. Phys.: Condens. Matter* **21**, 216001 (2009).
- [41] R. S. Fishman, J. T. Haraldsen, N. Furukawa, and S. Miyahara, *Phys. Rev. B* **87**, 134416 (2013).
- [42] Y. Yamaguchi, S. Tomiyoshi, M. Harada, and G. Shirane, *J. Magn. Magn. Mater.* **103**, 50 (1992).
- [43] R. Coehoorn and R. A. d. Groot, *J. Phys. F: Met. Phys.* **15**, 2135 (1985).
- [44] L. M. Sandratskii, R. F. Egorov, and A. A. Berdyshev, *Phys. Stat. Sol. (b)* **103**, 511 (1981).
- [45] P. E. Blöchl, *Phys. Rev. B* **50**, 17953 (1994).
- [46] G. Kresse and J. Hafner, *Phys. Rev. B* **48**, 13115 (1993).
- [47] G. Kresse and J. Furthmüller, *Phys. Rev. B* **54**, 11169 (1996).
- [48] G. Kresse and D. Joubert, *Phys. Rev. B* **59**, 1758 (1999).
- [49] S. L. Dudarev, G. A. Botton, S. Y. Savrasov, C. J. Humphreys, and A. P. Sutton, *Phys. Rev. B* **57**, 1505 (1998).
- [50] K. Momma and F. Izumi, *J. Appl. Crystallogr.* **44**, 1272 (2011).